crystals

MDPI

Article

Experimental Observation of Possible Pressure-Induced Phase Transformation in $GdAlO_3$ Perovskite Using In Situ X-ray Diffraction

Maria Mora [1], Andriy Durygin [1], Vadym Drozd [1], Shanece Esdaille [1], Jiuhua Chen [1,*], Surendra Saxena [1], Xue Liang [1] and Leonid Vasylechko [2]

[1] Center for the Study of Matter at Extreme Conditions (CeSMEC), Department of Mechanical and Materials Engineering, Florida International University, Miami, FL 33199, USA; mmora059@fiu.edu (M.M.); durygina@fiu.edu (A.D.); drozdv@fiu.edu (V.D.); sesdaill@fiu.edu (S.E.); saxenas@fiu.edu (S.S.); xlian002@fiu.edu (X.L.)

[2] Semiconductor Electronics Department, Lviv Polytechnic National University, 12 Bandera, 79013 Lviv, Ukraine; crystal-lov@polynet.lviv.ua

* Correspondence: chenj@fiu.edu; Tel.: +1-305-348-3140

Abstract: Gadolinium aluminate perovskite ($GdAlO_3$) was studied at high pressures of up to 23 GPa in a diamond anvil cell (DAC) using monochromatic synchrotron X-ray powder diffraction. Evidence of a pressure-induced phase transformation from orthorhombic (*Pbnm*) to rhombohedral ($R\bar{3}c$) structure was observed at 21 GPa and further proved by DFT calculations. Before phase transition, the volumetric ratio of polyhedron A and B (i.e., V_A/V_B for ABX_3 general notation) in the *Pbnm* phase continuously increased towards the ideal value of five at the transition, indicating a pressure-induced decrease in the structural distortion as opposed to the trend in many other orthorhombic perovskites (e.g., $CaSnO_3$, $CaGeO_3$, $MgSiO_3$ and $NaMgF_3$). Pressure–volume data of the *Pbnm* phase were fitted to the third-order Birch–Murnaghan equation of state yielding a bulk modulus (K_o) of 216 ± 7 GPa with a pressure derivative of the bulk modulus (K_o') of 5.8 GPa (fixed). This work confirms the pressure-induced phase transformation from orthorhombic to a higher symmetry structure previously predicted in $GdAlO_3$ perovskite.

Keywords: $GdAlO_3$; perovskite; high pressure; diamond anvil cell; bulk modulus; synchrotron X-ray diffraction; phase transition

check for updates

Citation: Mora, M.; Durygin, A.; Drozd, V.; Esdaille, S.; Chen, J.; Saxena, S.; Liang, X.; Vasylechko, L. Experimental Observation of Possible Pressure-Induced Phase Transformation in $GdAlO_3$ Perovskite Using In Situ X-ray Diffraction. *Crystals* **2023**, *13*, 1060. https://doi.org/10.3390/cryst13071060

Academic Editor: Catalin Popescu

Received: 30 May 2023
Revised: 28 June 2023
Accepted: 29 June 2023
Published: 5 July 2023

1. Introduction

Perovskite materials are well-known solids with the general formula of ABO_3, where A is a large cation occupying the voids with coordination number 12 (in the ideal cubic perovskite structure) and B is a smaller cation in octahedral oxygen coordination. Rare-earth aluminates with perovskite structure are potential materials for optical, electronic, structural, and magnetic applications such as colossal magneto resistant materials, substrates for high-temperature superconductors, solid oxide fuel cells and microwave dielectric materials [1–7]. A large number of rare-earth perovskite-type oxides have been studied because of their interesting properties. Many of those ABO_3 compounds crystallize into an orthorhombic structure which deviates from the ideal cubic structure via the titling and distortion of the BO_6 octahedra [8,9]. The distortion degree of perovskites can be described with the following parameters: the BO_6 octahedral tilting and rotation, the Goldschmidt's tolerance factor(t) and the polyhedron volume ratio V_A/V_B, where V_A is the volume of A-site polyhedron and V_B is that of the B-site octahedron. The values for the tilting angle (∢B–O1–B), the rotation angle (∢B–O2–B), t and V_A/V_B for an ideal perovskite are 180°, 180°, 1 and 5, respectively. The nature of this distortion has been related to the existence of different ionic radii within the crystal [10–16].

Pressure, as one of the important thermodynamic parameters plays a critical role in altering material properties. Under pressure, shortening of the effective ionic radius may vary depending on the ion itself and its coordinating environment. Zhao et al. [17] developed a model using the bond valence concept to predict the structural behavior of oxide perovskites at high pressure, introducing the ratio M_A/M_B, which determines the relative compressibility of the AO_{12} and BO_6 sites due to the change in the average bond distance, where M_A and M_B describe the variation of the bond valence sum at the central cation in a polyhedral site. Based on this model, the relative polyhedral compressibility (i.e., V_A/V_B) determines the influence of pressure on the crystal structure of perovskite [18]. Some orthorhombic rare-earth perovskites such as $LaFeO_3$ and $PrFeO_3$ undergo a first-order transition to high-pressure phases, among which the high-pressure phase of $LaFeO_3$ was reported to have a tetragonal symmetry with unknown structural details [19]. First-order reversible structural phase transition from the orthorhombic to rhombohedral $R\bar{3}c$ structure was observed in $SmAlO_3$ and $LaGaO_3$ near 10 GPa [20] and 2.5 GPa [21], respectively, by X-ray synchrotron powder diffraction.

$GdAlO_3$ orthorhombic perovskite has been studied as a potential material for industrial applications considering its magnetic, optical, electronic, and structural properties [22–27]. The crystal structure of gadolinium aluminate has been reported at ambient conditions [22,28,29]. Ross et al. [30,31] studied the structural behavior of $GdAlO_3$ at high pressures of up to 8 GPa and found that the abovementioned structural distortion decreases with increasing pressure. By extrapolating the metrical deviation of the orthorhombic perovskite from tetragonal symmetry (proportional to $(b-a)/a_0$ where a_0 is the value of the phase with a higher symmetry), they predicted an orthorhombic to higher-symmetry transition at about 12 GPa in $GdAlO_3$. Nevertheless, such a transition has never been directly observed in any experimental study. In this work, we compressed $GdAlO_3$ up to 23 GPa and observed signs of the predicted transition but at a higher pressure (21 GPa). Density functional theory (DFT) calculations indicate that the rhombohedral structure ($R\bar{3}c$) found in $LaGaO_3$ is favorable at high pressure over the low-pressure orthorhombic structure (*Pbnm*) of $GdAlO_3$ and the tetragonal structure ($I4/mcm$) found in $CeAlO_3$ [32].

2. Materials and Methods

The $GdAlO_3$ sample was prepared through the solid-state reaction of Gd_2O_3 and Al_2O_3 by arc-melting in argon atmosphere. Details of the procedure can be found elsewhere [9,32,33]. High pressures were generated using a Mao–Bell diamond anvil cell (DAC). Two opposed diamond anvils with 300 μm diameter culets were compressed on a 302 stainless steel gasket with an initial thickness of 250 μm. The gasket was pre-indented with the anvils to a thickness of 60 μm and a hole of a 125 μm diameter was drilled at the center of the indentation to hold the sample. The synthesized sample was grounded into fine powder in an agate mortar and loaded into the 125 μm diameter sample chamber. A methanol–ethanol (4:1) mixture was loaded together with the sample and a small ruby sphere (pressure calibrant) as a pressure transmitting medium. The in situ high-pressure powder X-ray diffraction experiments were performed at the 16-IDB beamline of HPCAT (High Pressure Collaborative Access Team) at Advanced Photon Source (APS) of Argonne National Laboratory, Lemont, IL, USA. The monochromatic X-ray beam of a 0.3757 Å wavelength was focused to a spot size of 5 μm. Diffraction patterns were recorded using a MAR345 detector. During the experiment, the sample pressure was increased stepwise; fluorescence of the ruby sphere and sample diffraction were collected at each step. The sample pressure was determined using ruby fluorescence pressure scale [34,35]. The FIT2D software [36] was used to integrate the recorded 2-dimensional diffraction patterns to obtain intensity versus 2θ plots. Rietveld refinements were performed for both the ambient-pressure phase and the high-pressure phase at 21 GPa using the GSAS software with a GUI interface [37,38]. The volumetric compression data of the ambient-pressure phase were derived through full-spectrum Le Bail analysis of the in-situ X-ray diffraction patterns.

Density functional theory (DFT) calculations were performed using the Vienna ab initio simulation package (VASP 6.3) [39,40]. The generalized gradient approximation (GGA) [41] with the Perdew–Burke–Ernzerhof (PBE) exchange–correlation functional [42] was used to describe exchange and correlation effects. Electron wave functions were expanded by a plane wave with a cutoff energy of 520 eV. The Gaussian smearing method was used with a width of 0.05 eV. A Monkhorst–Pack [43] k-point grid was set with a 0.03 1/Å k-point separation which provides a mesh density of >1000 per reciprocal atom. Atomic relaxation was performed until the changes in the electronic and ionic steps were less than 10^{-6} eV and 10^{-5} eV, respectively.

3. Results

A sequence of in situ X-ray diffraction patterns of the sample was taken up to 23 GPa (Figure 1). All the diffraction peaks in the initial diffraction pattern were identified as the *Pbnm* perovskite phase in agreement with previous works [9,29,31,44]. Disappearance of (111), (021), (113), (023)/(221), and (133) peaks indicates a possible pressure-induced structural phase transition at a pressure between 16.2 GPa and 21 GPa, and this transition is reversible as all these disappeared peaks reappear when the pressure is released back to ambient. From the symmetry relationship point of view, there are three higher symmetry phases for perovskite in the pathway from its *Pbnm* orthorhombic to $Pm\bar{3}m$ cubic polymorphs, i.e., *P4/mbm*, *I4/mcm* and $R\bar{3}c$ [16]. However, differences in symmetry operations require that the (111) and (021) peaks in the *Pbnm* orthorhombic phase disappear in the *I4/mcm* tetragonal phase (i.e., hkl: h + k + l = 2n and 0kl: k, l = 2n) and the $R\bar{3}c$ rhombohedral phase while they are allowed in the *P4/mbm* tetragonal phase. Since the (111) and (021) peaks in the *Pbnm* orthorhombic phase completely disappeared when sample pressure increased to 21 GPa (Figure 1), the *P4/mbm* tetragonal phase was not considered. Therefore, we examined three possible structural models using the diffraction pattern at 21 GPa, i.e., *Pbnm* (the ambient pressure phase), $R\bar{3}c$ (the high-pressure phase observed in $SmAlO_3$ [20] and *I4/mcm* (the structure of $CeAlO_3$). As shown in Figure 2 and Table 1, the differences in structure refinements using the three different space groups are not significant enough to conclusively determine the favorable structure for the high-pressure phase. We then calculated the total energy of the three structure models as a function of pressure using DFT (Figure 3). The calculation results indicate that *Pbnm* is favorable at low pressures, whereas $R\bar{3}c$ is favorable at high pressures, although the calculated transition pressure (75 GPa) is much higher than the experimental pressure where the disappearance of diffraction peaks was observed. We realize that the methanol–ethanol (4:1) pressure medium solidifies at a pressure above 10 GPa [45], creating a non-hydrostatic pressure environment and therefore the sample may experience significant stresses at 21 GPa. Zhao et al. [46,47] were able to quantify the stress field using single-crystal X-ray diffraction and indicate that such a non-hydrostatic pressure environment in a DAC may affect and even induce the phase transition as stress fields can influence the structural distortions in perovskites. A more recent experimental study [48] demonstrated that applying non-hydrostatic pressure may lower the transition pressure in a DAC. Taking this stress influence and possibly large uncertainty in determining transition pressure using DFT calculations into consideration, we propose that the theoretically predicted *Pbnm* to $R\bar{3}c$ phase transition may occur at a pressure between 16.2 GPa and 21 GPa promoted by non-hydrostatic pressure. As shown in Table 1, the volume per formula unit of the $R\bar{3}c$ structure is nearly identical to the *Pbnm* structure within the experimental uncertainty. To further confirm the symmetry of the high-pressure phase, higher resolution structure characterization, e.g., in situ single crystal X-ray diffraction, is needed.

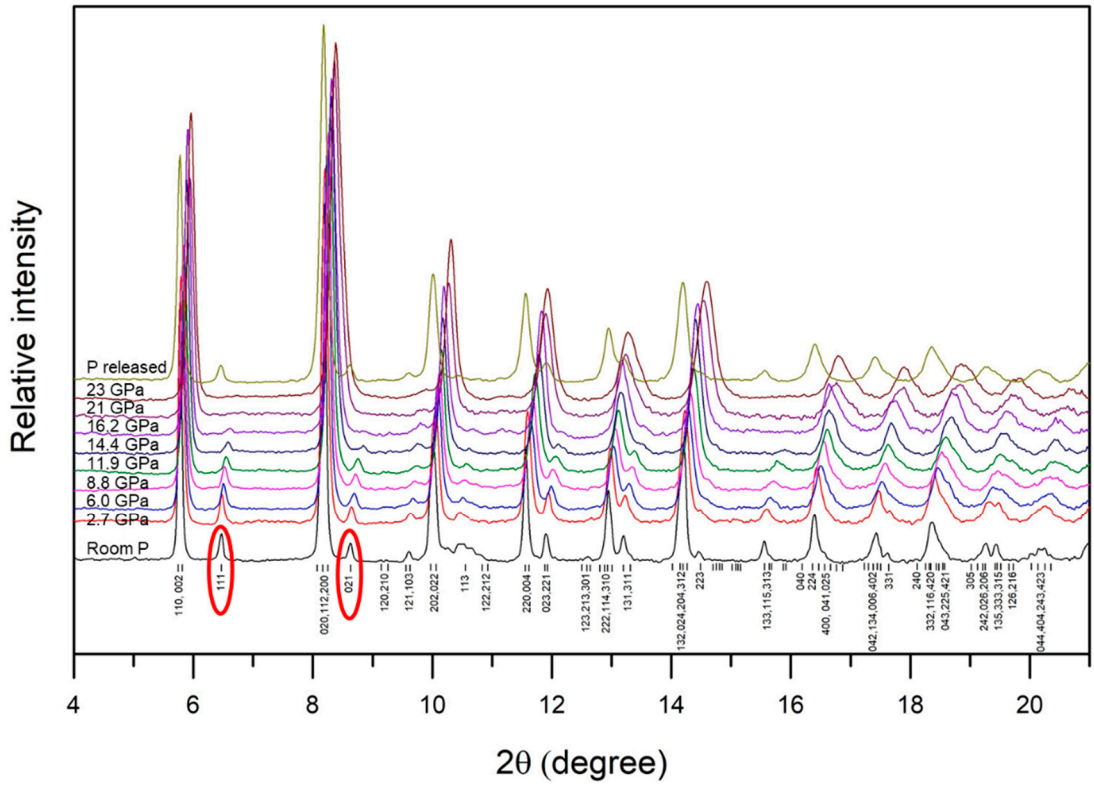

Figure 1. In situ synchrotron X-ray diffraction patterns of $GdAlO_3$ at different pressures as indicated and room temperature (λ = 0.3757 Å). Red circles indicate the characteristic peaks that disappear when *Pbnm* to $R\bar{3}c$ phase transition occurs.

Table 1. Results of Rietveld refinement of the diffraction pattern of $GdAlO_3$ at 21 GPa using *Pbnm*, *I*4/*mcm* and $R\bar{3}c$ space groups.

	Atom	x	y	Z	*a* (Å)	*b* (Å)	*c* (Å)	V (Å^3)	V/Z (Å^3)	wR
Pbnm	Gd	0.998(7)	0.003(4)	0.25	5.093(1)	5.146(1)	7.322(1)	191.89(2)	47.97	2.9%
	Al	0	0.5	0						
	O1	0.5(4)	0.98(18)	0.25						
	O2	0.75(8)	0.25(10)	0.00(7)						
*I*4/*mcm*	Gd	0	0.5	0.25	5.123(2)	5.123(2)	7.25(1)	190.76(4)	47.69	1.9%
	Al	0	0	0						
	O1	0	0	0.25						
	O2	0.32(5)	0.82(5)	0						
$R\bar{3}c$	Gd	0	0	0	5.111(2)	5.111(2)	12.713(5)	287.55(21)	47.93	2.9%
	Al	0.421(3)	0	0.25						
	O1	0	0	0.25						

The structural deviation of the perovskite (ABX_3) structure from its ideal cubic structure is commonly characterized by its BX_6 octahedral titling. The *Pbnm* perovskite has a simple tilt system of $a^-a^-c^+$ [49,50] (the superscript + and − indicate that successive octahedra along an axis have the same tilt and opposite tilt respectively). Figure 3a shows the $GdAlO_3$ structure model based on the refinement of the X-ray diffraction at ambient condition. The tilting angles along the *a*-axis and the *b*-axis are identical, and successive octahedra along each of these axes have opposite tilt, whereas successive octahedra along the *c*-axis have the same tilt. The $R\bar{3}c$ perovskite has a tilt system of $a^-a^-a^-$ [49,50]. Figure 3b shows the high-pressure phase structure model of $GdAlO_3$ based on the refinement of the X-ray diffraction at 21 GPa. There are three identical tilts along the *a*, *b* and *c*-axis, and successive octahedra along each of the axes have opposite tilt. The degree of structure

distortion of perovskite can be evaluated using the volumetric ratio (V_A/V_B) between AX_{12} and BX_6 polyhedron with an ideal value of five for undistorted cubic structure [15]. Assuming regular BX_6 octahedra throughout the *Pbnm* perovskite structure, V_A and V_B can be calculated through its unit cell dimensions [15,51]. Evolution of the V_A/V_B ratio of the low-pressure phase in $GdAlO_3$ with pressure is given in Figure 4 shows the V_A/V_B ratio as a function of pressure (Table 2). As pressure increases, the V_A/V_B ratio of the *Pbnm* phase approaches the value of five, indicating a transition to a higher symmetry. Note that during the phase transition (between 16.2 and 21 GPa), V_A/V_B goes beyond five at 16.2 GPa, indicating large pre-transition straining. Detailed reasoning for these phenomena is unclear. While coexistence of two phases may compromise refinement accuracy, simultaneously fitting two phases did not solve this issue in the *Pbnm* phase. Although the pure high-pressure phase was observed at 21 GPa, the transition likely starts at 16.2 GPa since significant weakening of (111), (021), (113), (023)/(221), and (133) peaks occurs at this pressure, which is still higher than the transition pressure (12 GPa) predicted by Ross et al. [30,31].

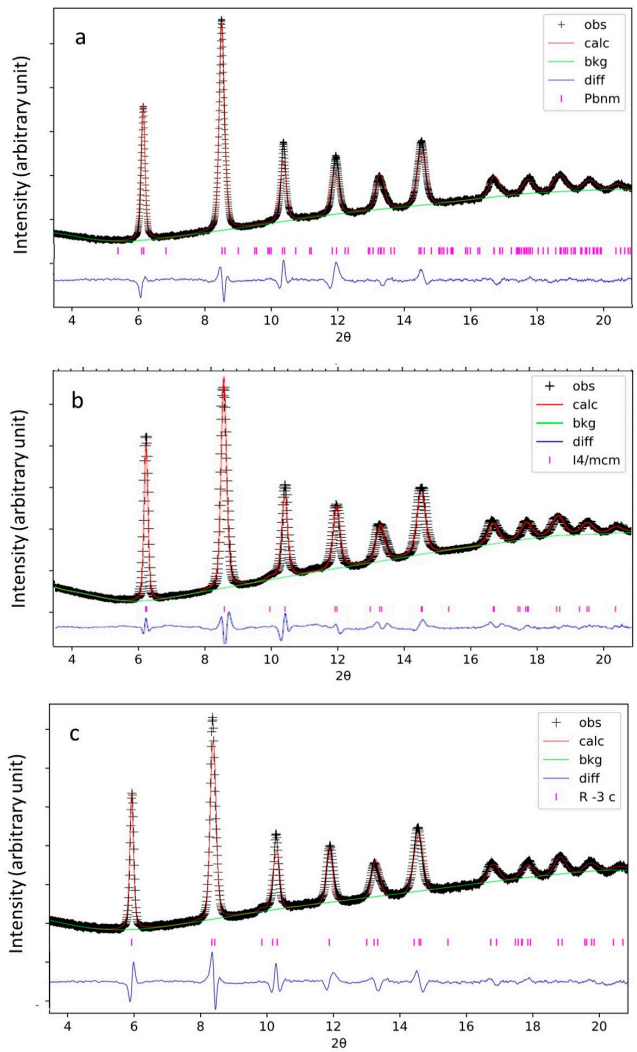

Figure 2. Result of Rietveld refinement of the diffraction pattern of $GdAlO_3$ at 21 GPa with (**a**) *Pbnm*, (**b**) *I*4/*mcm* and (**c**) $R\bar{3}c$ space groups. Crosses are experimentally observed data, red solid line is calculated data, vertical bars are locations of expected diffraction peaks, and blue line at the bottom is the difference between the observed and calculated data.

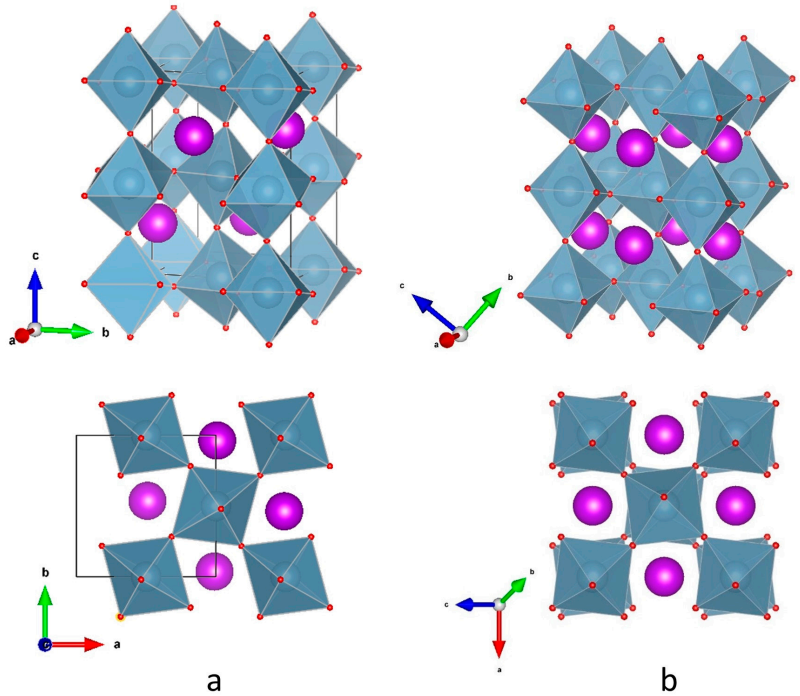

Figure 3. Crystal structure of $GdAlO_3$ at (**a**) ambient pressure (*Pbnm* space group, $a^-a^-c^+$ tilt system), and (**b**) 21 GPa ($R\bar{3}c$ space group, $a^-a^-a^-$ tilt system). Solid black lines indicate unit cell. Small red dots represent oxygen atoms and large pink spheres gadolinium atoms. Grey areas denote AlO_6 octahedra.

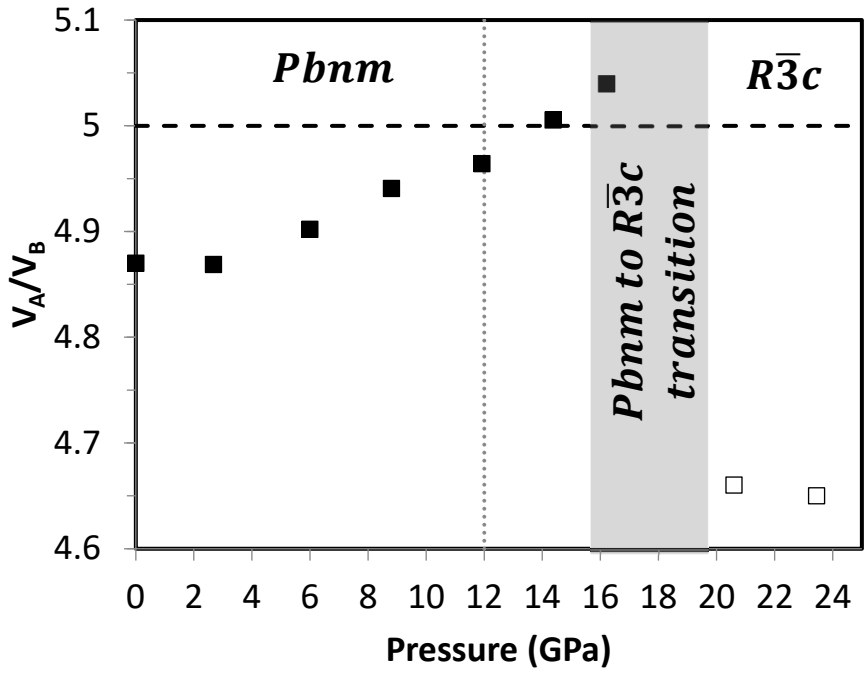

Figure 4. Variations of V_A/V_B of the *Pbnm* (solid symbols) and $R\bar{3}c$ (open symbols) phase of $GdAlO_3$ as a function of pressure. The broken line indicates the ideal value of V_A/V_B for undistorted cubic perovskite structure. The dotted line indicates the pressure of the predicted structural transition to from *Pbnm* to a higher symmetry [30,31]. The shaded area shows the pressure range where the *Pbnm* to $R\bar{3}c$ transition may actually happen under non-hydrostatic pressure.

Table 2. Unit cell parameters of $GdAlO_3$ measured in the diamond anvil cell from 1 bar to 23 GPa. The figures in parentheses represent 1 esd of the last decimal place shown.

	P (GPa)	σ * (GPa)	*a* (Å)	*b* (Å)	*c* (Å)	V (Å^3)	V_a/V_b **
Pbnm	0.00	0	5.2534(7)	5.2910(6)	7.458(1)	207.29(1)	4.87
	2.7	0.3	5.2289(9)	5.2823(6)	7.401(2)	204.4(2)	4.87
	6.0	0.5	5.212(1)	5.2558(8)	7.368(2)	201.82(2)	4.90
	8.8	0.8	5.2050(7)	5.2373(8)	7.352(1)	200.42(1)	4.94
	11.9	1.0	5.188(1)	5.218(1)	7.316(2)	198.06(3)	4.96
	14.4	1.0	5.173(4)	5.176(3)	7.308(3)	195.64(3)	5.01
	16.2	1.2	5.175(1)	5.120(1)	7.371(1)	195.29(3)	5.04
$R\bar{3}c$	20.6	2.0	5.111(2)	5.111(2)	12.713(5)	287.55(21)	4.66
	23.4	2.0	5.094(1)	5.094(1)	12.682(3)	285.02(6)	4.65

* Experimental uncertainty taking the nonhydrostatic pressure due to solidification of pressure medium into account [45]. ** V_a and V_b are calculated from the unit cell dimensions.

The compression data (Figure 5) show that the transition from the *Pbnm* to $R\bar{3}c$ phase in $GdAlO_3$ at a pressure between 16.2 GPa and 21 GPa accompanied nearly no volumetric discontinuity. Nevertheless, the space group–subgroup theory indicates that the *Pbnm* to $R\bar{3}c$ transformation is a first-order phase transition [16]. Likely, the volumetric discontinuity is so small that it is unrecognizable with the experimental uncertainty of this study. The orthorhombic (*Pnma*) to rhombohedral ($R\bar{3}c$) transition observed in $GdAlO_3$ and $LaGaO_3$ has a similar unrecognizable volume discontinuity [20,21].

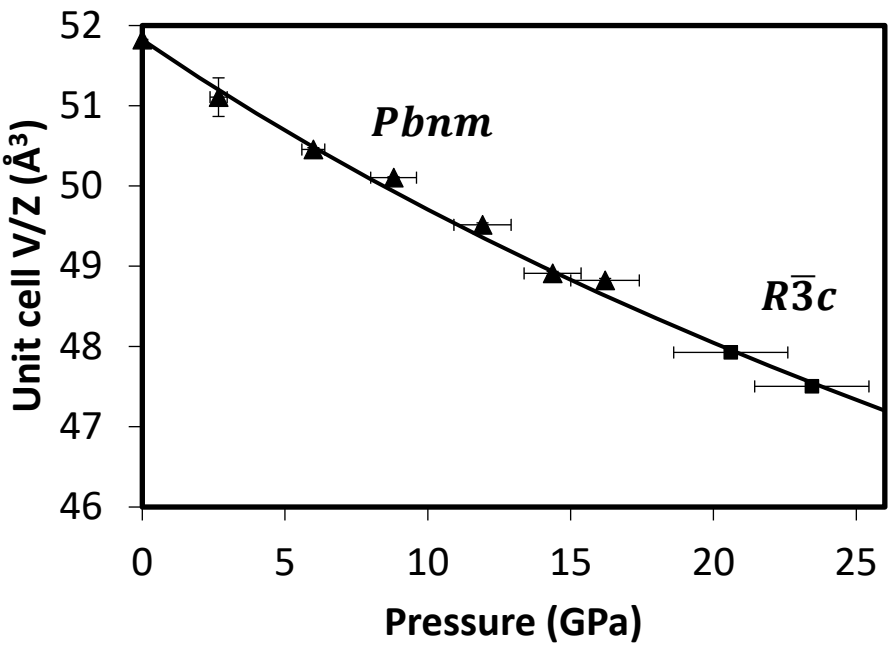

Figure 5. Variation of the volume per formula unit of $GdAlO_3$ perovskite (triangles: the *Pbnm* phase, squares: the $R\bar{3}c$ phase) as a function of pressure. The experimental errors are either indicated by the bars or less than the size of the symbols. The solid line represents the third-order Birch–Murnaghan EoS fitting for the data of the *Pbnm* phase (triangles).

The obtained volumetric data of the *Pbnm* phase were fitted into the third–order Birch–Murnaghan equation of state (EoS) [52]:

$$P = \frac{3}{2}K_0\left[\left(\frac{V}{V_0}\right)^{-7/3} - \left(\frac{V}{V_0}\right)^{-5/3}\right] x \left\{1 + \frac{3}{4}(K_o' - 4))\left[\left(\frac{V}{V_0}\right)^{-2/3} - 1\right]\right\},$$

where P is the pressure applied, V is the volume of the unit cell under pressure, K_0 is the bulk modulus, subscript 0 indicates the ambient pressure, and K_0' is the pressure derivative of bulk modulus. EoSFit 7.0 software [53] was used for fitting the experimental P–V data into the EoS. The fitting was weighted according to the uncertainty of each point [53] and K_0' was fixed at 5.8 based on the previous experimental data by Ross et al. [31]. The V_0 and K_0 determined through the fitting are 207.29 ± 0.01 Å^3 and 216 ± 7 GPa, respectively. Due to the very limited data for the high-pressure $R\bar{3}c$ phase (only two points), no EoS fitting was performed.

4. Discussion

While temperature influence on the structure of perovskite has been extensively studied, investigations of pressure influence on perovskite structure are still limited. Pressure influence on the *Pbnm* perovskite structure is twofold. Some structural studies on $MgSiO_3$ [54,55] and $NaMgF_3$ [11,56] perovskite showed that the V_A/V_B ratio of the *Pbnm* perovskite structure decreases further away from the ideal value of five upon compression, i.e., pressure increases the distortion of the perovskite. Experimental studies of pressure effect on $CaGeO_3$ perovskite structure presented controversial results. In situ extended X-ray absorption fine structure (EXAFS) study inferred a trend of reduced distortion under high pressure [57], while X-ray diffraction study indicated a reversed pressure effect [58]. Controversial results about the pressure influence also exist in theoretical calculations on $CaSiO_3$ perovskite [59,60]. $CaSnO_3$ is another example of perovskites that show increased distortion with increasing pressure [61]. Whether pressure enhances the distortion or reduces it depends on the relative compressibility of the AX_6 octahedra and the BX_{12} polyhedron. In the case of $GdAlO_3$ of this study, the GdO_6 octahedra are less compressible than the AlO_{12} polyhedron, yielding an increase in the V_A/V_B ratio towards five. This is consistent with previous single-crystal X-ray diffraction study on $GdAlO_3$ by Ross et al. [30,31], although their experiment was limited to the high pressure of 8 GPa and therefore did not observe any phase transition. An ab initio calculation [62] and a single-crystal X-ray diffraction study [63] on another rare-earth aluminate perovskite, $YAlO_3$, also show that the AX_6 octahedra are less compressible than the BX_{12} polyhedron. All of these align nicely with the model developed by Zhao et al. [17] which shows that in $GdFeO_3$-type orthorhombic perovskites with both cations possessing a formal charge of 3+, the structural distortion decreases with increasing pressure and the structure evolves towards a higher symmetry at high pressure.

The bulk modulus (216 GPa) of *Pbnm* $GdAlO_3$ derived in this study is higher than those reported previously by Bass et al. [64] using Brillouin spectroscopy (204 GPa) and by Ross et al. [31] using single-crystal X-ray diffraction (191 GPa). In perovskite-structured alkaline earth silicates, germanates, and titanates, a simple trend of a smaller unit formula volume leading to a larger bulk modulus has been observed [65]. In the case of rare-earth aluminate perovskite, a summary of the available bulk moduli is listed in Table 3. Figure 6 shows a plot of the bulk moduli at ambient conditions as a function of ionic radius of R^{3+} [66] in the rare-earth aluminate perovskite $RAlO_3$ (R = La, Pr, Nd, Sm, Eu and Gd). The linear trendline defined by the data of $LaAlO_3$, $PrAlO_3$, $NdAlO_3$, $SmAlO_3$ and $EuAlO_3$ indicates that the bulk modulus of $RAlO_3$ increases as the ionic radius of R^{3+} decreases. The bulk modulus value of $GdAlO_3$ derived from the current study agrees well with the general trend of bulk moduli as a function of the ionic radius (Figure 6). More systematic studies on the bulk moduli of the perovskite-structured $RAlO_3$ aluminates for the entire rare-earth family will be interesting to generalize the influence of ionic radius on bulk modulus of the rare-earth aluminate perovskite. We also realize that the methanol–ethanol pressure medium may yield non-hydrostatic environment when the pressure rises above 10 GPa due to solidification [45]. Although enlarged experimental uncertainties because of the non-hydrostatic pressure have been taken into account through weighted EoS fitting, a future study using nearly hydrostatic pressure medium such as helium or neon is more desirable for a better characterization of the compression behavior and the phase transition.

Table 3. Summary of the available bulk moduli (K) of rare-earth aluminate perovskite $RAlO_3$.

Composition	Space Group	K (GPa)	Reference	Note	Use for the Trendline
$LaAlO_3$	$R\bar{3}c$	190 ± 5	[67]	XRD, fit using $Pm\bar{3}m$, up to 40 GPa (improper space group and pressure range)	no
$LaAlO_3$	$R\bar{3}c$	177 ± 4	[68]	XRD, up to 7 GPa	yes
$LaAlO_3$	$R\bar{3}c$	196	[69]	Brillouin scattering	yes
$PrAlO_3$	*Pnma*	193 ± 1	[70]	XRD, up to 7 GPa	yes
$NdAlO_3$	$R\bar{3}c$	204	[71]	*Ab-initio* calculation	yes
$SmAlO_3$	*Pnma*	178 ± 14	[72]	Ultrasound, at 0.6 GPa, 2.2% porosity	no
$SmAlO_3$	*Pnma*	198 ± 4	[64]	Brillouin scattering	yes
$EuAlO_3$	*Pnma*	203 ± 15	[72]	Ultrasound, at 0.6 GPa, 2.4% porosity	no
$EuAlO_3$	*Pnma*	213	[73]	Ultrasound, sample of [72], corrected for porosity	yes
$GdAlO_3$	*Pnma*	179 ± 15	[72]	Ultrasound, at 0.6 GPa, 2.4% porosity	no
$GdAlO_3$	*Pnma*	203 ± 4	[64]	Brillouin scattering	no
$GdAlO_3$	*Pnma*	191 ± 1	[31]	XRD, up to 8 GPa	no
$GdAlO_3$	*Pnma*	216 ± 7	this study	XRD, up to 16 GPa	no

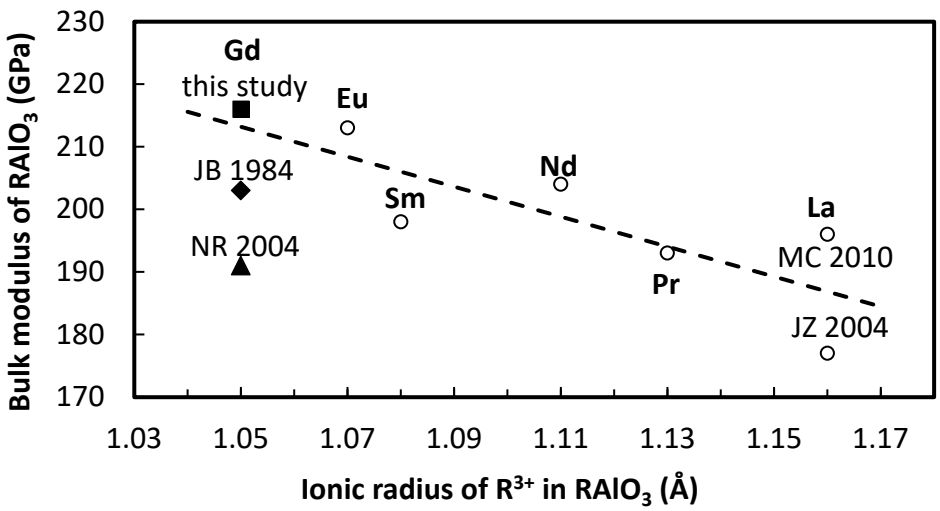

Figure 6. Bulk moduli of rare-earth aluminate perovskite $RAlO_3$ (R = La, Pr, Nd, Sm, Eu and Gd) as a function of the ionic radius of R^{3+}. The broken line represents the linear trendline based on the data of $LaAlO_3$ (JZ 2004 [68], MC 2010 [69]), $PrAlO_3$ [70], $NdAlO_3$ [71], $SmAlO_3$ [64] and $EuAlO_3$ [73]. Data for $GdAlO_3$ of this study, JB 1984 [64] and NR 2004 [31] are plotted to show the agreement of these data with the linear trendline.

5. Conclusions

The previously predicted pressure-induced phase transformation from orthorhombic (*Pbnm*) to a higher-symmetry structure in $GdAlO_3$ has been observed in in situ X-ray diffraction and the higher-symmetry phase is identified with space group of $R\bar{3}c$ with the assistant of DFT calculations. The X-ray diffraction patterns indicate that the structural phase transformation occurs between 16 and 21 GPa, although the volumetric variations V_A/V_B of the *Pbnm* phase suggest the transition to a higher symmetry may apparently start at around 14 GPa. The structural phase transformation is a first-order transition according to the space groups but the volumetric discontinuity is indistinguishable with the experimental uncertainty of the current study. A bulk modulus (K_0) of 216 ± 7 GPa with a fixed derivative bulk modulus (K_0') at 5.8 was obtained for the *Pbnm* phase according to the third-order Birch–Murnaghan equation of state. The bulk modulus derived in this study is higher than the previously reported values but is in good agreement with the linear trend of increase in bulk modulus as the ionic radius of R^{3+} in rare-earth aluminate perovskite $RAlO_3$ decreases.

Author Contributions: Conceptualization, J.C., S.S. and L.V.; Data curation, M.M.; Formal analysis, M.M., V.D. and J.C.; Funding acquisition, J.C.; Investigation, M.M., A.D., V.D., S.E., J.C., S.S., X.L. and L.V.; Methodology, M.M., A.D. and V.D.; Project administration, A.D. and V.D.; Resources, J.C. and S.S.; Supervision, J.C.; Validation, M.M. and X.L.; Visualization, S.E. and J.C.; Writing—original draft, M.M.; Writing—review and editing, S.E., J.C. and L.V. All authors have read and agreed to the published version of the manuscript.

Funding: The research was supported in part by NSF Grant No. EAR-1723185.

Institutional Review Board Statement: Not applicable.

Informed Consent Statement: Not applicable.

Data Availability Statement: The data presented in this study are available on request from the corresponding author.

Acknowledgments: We thank Lyci George for her assistance in data collection. Portions of this work were performed at HPCAT (Sector 16), Advanced Photon Source (APS), Argonne National Laboratory. HPCAT operations are supported by DOE-NNSA's Office of Experimental Sciences. The Ad-vanced Photon Source is a U.S. Department of Energy (DOE) Office of Science User Facility operated for the DOE Office of Science by Argonne National Laboratory. L. Vasylechko acknowledges the support of the National Research Foundation of Ukraine under grant no. 2020.02/0373 "Crystalline phosphors' engineering for biomedical applications, energy saving lighting and contactless thermometry".

Conflicts of Interest: The authors declare no conflict of interest. The funder had no role in the design of the study; in the collection, analyses, or interpretation of data; in the writing of the manuscript, or in the decision to publish the results.

References

1. Cho, S.-Y.; Kim, I.-T.; Hong, K.S. Microwave dielectric properties and applications of rare-earth aluminates. *J. Mater. Res.* **1999**, *14*, 114–119. [CrossRef]
2. Henke, M.; Perbon, J.; Kuck, S. Preparation and spectroscopy of Yb^{2+}-doped $Y_3Al_5O_{12}$, $YAlO_3$, and $LiBaF_3$. *J. Lumin.* **2000**, *87*, 1049–1051. [CrossRef]
3. Jin, H.; Rhim, S.H.; Im, J.; Freeman, A.J. Topological oxide insulator in cubic perovskite structure. *Sci. Rep.* **2013**, *3*, 1651. [CrossRef] [PubMed]
4. Lepe, F.J.; Fernández-Urbán, J.; Mestres, L.; Martínez-Sarrión, M.L. Synthesis and electrical properties of new rare-earth titanium perovskites for SOFC anode applications. *J. Power Sour.* **2005**, *151*, 74–78. [CrossRef]
5. Lybye, D.; Bonanos, N. Proton and oxide ion conductivity of doped $LaScO_3$. *Solid State Ion.* **1999**, *125*, 339–344. [CrossRef]
6. Lybye, D.; Poulsen, F.W.; Mogensen, M. Conductivity of A- and B-site doped $LaAlO_3$, $LaGaO_3$, $LaScO_3$ and $LaInO_3$ perovskites. *Solid State Ion.* **2000**, *128*, 91–103. [CrossRef]
7. Pickett, W.E.; Singh, D.J. Electronic structure and half-metallic transport in the La1-xCaxMnO$_3$ system. *Phys. Rev. B* **1996**, *53*, 1146–1160. [CrossRef]
8. Vasylechko, L.; Senyshyn, A.; Bismayer, U. *Perovskites-Types Aluminates and Gallates*; Gschneidner, K.A., Jr., Bünzli, J.C.G., Pechersky, V.K., Eds.; Elesvier, B.V.: Amsterdam, The Netherlands, 2009; Volume 39, pp. 113–295.
9. Vasylechko, L.; Shmanko, H.; Ohon, N.; Prots, Y.; Hoffmann, S.; Ubizskii, S. Lattice crossover and phase transitions in $NdAlO_3$—$GdAlO_3$ system. *J. Solid State Chem.* **2013**, *198*, 101–107. [CrossRef]
10. Avdeev, M.; Caspi, E.N.; Yakovlev, S. On the polyhedral volume ratios V_A/V_B in perovskites ABX_3. *Acta Crystallogr. Sect. B Struct. Sci.* **2007**, *63*, 363–372. [CrossRef]
11. Chen, J.; Liu, H.; Martin, C.D.; Parise, J.B.; Weidner, D.J. Crystal chemistry of $NaMgF_3$ perovskite at high pressure and temperature. *Am. Mineral.* **2005**, *90*, 1534–1539. [CrossRef]
12. Goldschmidt, V.M. The Laws of Crystal Chemistry (Die Gesetze der Krystallochemie). *Die Nat.* **1926**, *14*, 477–485. [CrossRef]
13. Jacobsson, T.J.; Pazoki, M.; Hagfeldt, A.; Edvinsson, T. Goldschmidt's Rules and Strontium Replacement in Lead Halogen Perovskite Solar Cells: Theory and Preliminary Experiments on $CH_3NH_3SrI_3$. *J. Phys. Chem. C* **2015**, *119*, 25673–25683. [CrossRef]
14. Magyari-Köpe, B.; Vitos, L.; Johansson, B.; Kollár, J. Origin of octahedral tilting in orthorhombic perovskites. *Phys. Rev. B* **2002**, *66*, 092103. [CrossRef]
15. Thomas, N.W. The compositional dependence of octahedral tilting in orthorhombic and tetragonal perovskites. *Acta Crystallogr. Sect. B Struct. Sci.* **1996**, *52*, 16–31. [CrossRef]
16. Thomas, N.W. A New Global Parameterization of Perovskite Structures. *Acta Crystallogr. Sect. B Struct. Sci.* **1998**, *B54*, 585–599.
17. Zhao, J.; Ross, N.L.; Angel, R.J. New view of the high-pressure behaviour of $GdFeO_3$-type perovskites. *Acta Crystallogr. Sect. B Struct. Sci.* **2004**, *60*, 263–271. [CrossRef]
18. Angel, R.J.; Ross, N.L.; Zhao, J. The compression of framework minerals: Beyond rigid polyhedra. *Eur. J. Mineral.* **2005**, *17*, 193–200. [CrossRef]

19. Xu, W.M.; Naaman, O.; Rozenberg, G.K.; Pasternak, M.P.; Taylor, R.D. Pressure-induced breakdown of a correlated system: The progressive collapse of the Mott-Hubbard state in $RFeO_3$. *Phys. Rev. B* **2001**, *64*, 094411. [CrossRef]
20. Li, H.; Ma, S.; Ye, J.; Li, N.; Wang, X. The effects of pressure on the lattice of the rare-earth-based perovskite-type oxides $SmAlO_3$ and $NdAlO_3$. *New J. Phys.* **2022**, *24*, 113008. [CrossRef]
21. Kennedy, B.J.; Vogt, T.; Martin, C.D.; Parise, J.B.; Hriljac, J.A. Pressure-induced orthorhombic to rhombohedral phase transition in $LaGaO_3$. *J. Phys. Condens. Matter* **2001**, *13*, L925. [CrossRef]
22. Du Boulay, D.; Lshizawa, N.; Maslen, E.N. $GdAlO_3$ perovskite. *Acta Crystallogr. Sect. C Cryst. Struct. Commun.* **2004**, *60*, i120–i122. [CrossRef]
23. Mahana, S.; Manju, U.; Topwal, D. Giant magnetocaloric effect in $GdAlO_3$ and a comparative study with $GdMnO_3$. *J. Phys. D Appl. Phys.* **2017**, *50*, 035002. [CrossRef]
24. Oliveira, H.H.S.; Cebim, M.A.; Da Silva, A.A.; Davolos, M.R. Structural and optical properties of $GdAlO_3$:RE^{3+} (RE = Eu or Tb) prepared by the Pechini method for application as X-ray phosphors. *J. Alloys Compd.* **2009**, *488*, 619–623.
25. Qiu, L.M.; Numazawa, T.; Thummes, G. Performance improvement of a pulse tube cooler below 4 K by use of $GdAlO_3$ regenerator material. *Cryogenics* **2001**, *41*, 693–696. [CrossRef]
26. Watras, A.; Pazik, R.; Dereń, P.J. Optical properties of Ce^{3+} doped ABO_3 perovskites (A = La, Gd, y and B = Al, Ga, Sc). *J. Lumin.* **2013**, *133*, 35–38. [CrossRef]
27. Su, H.; Shen, Z.; Ma, W.; Liu, Y.; Zhao, D.; Guo, Y. Comprehensive microstructure regularization mechanism and microstructure–property stability at 1773 K of directionally solidified $Al_2O_3/GdAlO_3$ eutectic ceramic composite. *Compos. Part B Eng.* **2023**, *256*, 110647. [CrossRef]
28. Geller, S.; Balla, V. Crystallographic studies of perovskite-like compounds. I. Rare earth orthoferrites and $YFeO_3$, $YCrO_3$, $YAlO_3$. *Acta Crystallogr.* **1956**, *9*, 1019–1025. [CrossRef]
29. Vasylechko, L.; Matkovskii, A.; Senyshyn, A.; Savytskii, D.; Knapp, M.; Bähtz, C. Crystal structure and thermal expansion of orthorhombic perovskite—Type RE aluminates. *HASYLAB Ann. Rep.* **2003**, *1*, 251–252.
30. Ross, N.L.; Zhao, J.; Angel, R.J. High-pressure structural behavior of $GdAlO_3$ and $GdFeO_3$ perovskites. *J. Solid State Chem.* **2004**, *177*, 3768–3775. [CrossRef]
31. Ross, N.L.; Zhao, J.; Burt, J.B.; Chaplin, T.D. Equations of state of $GdFeO_3$ and $GdAlO_3$ perovskites. *J. Phys. Condens. Matter* **2004**, *16*, 5721–5730. [CrossRef]
32. Vasylechko, L.; Senyshyn, A.; Trots, D.; Niewa, R.; Schnelle, W.; Knapp, M. $CeAlO_3$ and $Ce_{1-x}R_xAlO_3$ (R = La, Nd) solid solutions: Crystal structure, thermal expansion and phase transitions. *J. Solid State Chem.* **2007**, *180*, 1277–1290. [CrossRef]
33. Ohon, N.; Vasylechko, L.; Prots, Y.; Schmidt, M. Phase and structural behavior of $SmAlO_3$–$RAlO_3$ (R = Eu, Gd) systems. *Mater. Res. Bull.* **2014**, *50*, 509–513. [CrossRef]
34. Mao, H.K.; Xu, J.A.; Bell, P.M. Calibration of the ruby pressure gauge to 800 kbar under quasi-hydrostatic conditions. *J. Geophys. Res.* **1986**, *91*, 4673–4676.
35. Sokolova, T.S.; Dorogokupets, P.I.; Litasov, K.D. Self-consistent pressure scales based on the equations of state for ruby, diamond, MgO, B2–NaCl, as well as Au, Pt, and other metals to 4 Mbar and 3000 K. *Russ. Geol. Geophys.* **2013**, *54*, 181–199. [CrossRef]
36. Hammersley, A. FIT2D: A multi-purpose data reduction, analysis and visualization program. *J. Appl. Crystallogr.* **2016**, *49*, 646–652. [CrossRef]
37. Larson, A.C.; Dreele, R.B.V. *General Structure Analysis System (GSAS)*; Los Alamos National Laboratory Report LAUR 86–748; Los Alamos National Laboratory: Los Alamos, NM, USA, 2004; p. 224.
38. Toby, B.H. A graphical user interface for GSAS. *J. Appl. Cryst.* **2001**, *34*, 210–213.
39. Kresse, G.; Furthmüller, J. Efficient iterative schemes for ab initio total-energy calculations using a plane-wave basis set. *Phys. Rev. B* **1996**, *54*, 11169–11186. [CrossRef]
40. Kresse, G.; Furthmüller, J. Efficiency of ab-initio total energy calculations for metals and semiconductors using a plane-wave basis set. *Comput. Mater. Sci.* **1996**, *6*, 15–50. [CrossRef]
41. Perdew, J.P.; Chevary, J.A.; Vosko, S.H.; Jackson, K.A.; Pederson, M.R.; Singh, D.J.; Fiolhais, C. Atoms, molecules, solids, and surfaces: Applications of the generalized gradient approximation for exchange and correlation. *Phys. Rev. B* **1992**, *46*, 6671–6687. [CrossRef]
42. Perdew, J.P.; Burke, K.; Ernzerhof, M. Generalized Gradient Approximation Made Simple. *Phys. Rev. Lett.* **1996**, *77*, 3865–3868. [CrossRef] [PubMed]
43. Monkhorst, H.J.; Pack, J.D. Special points for Brillouin-zone integrations. *Phys. Rev. B* **1976**, *13*, 5188–5192. [CrossRef]
44. Chaudhury, S.; Parida, S.C.; Pillai, K.T.; Singh Mudher, K.D. High-temperature X-ray diffraction and specific heat studies on $GdAlO_3$, $Gd_3Al_5O_{12}$ and $Gd_4Al_2O_9$. *J. Solid State Chem.* **2007**, *180*, 2393–2399. [CrossRef]
45. Klotz, S.; Chervin, J.C.; Munsch, P.; Le Marchand, G. Hydrostatic limits of 11 pressure transmitting media. *J. Phys. D Appl. Phys.* **2009**, *42*, 075413. [CrossRef]
46. Zhao, J.; Angel, R.; Ross, N. Effects of deviatoric stresses in the diamond-anvil pressure cell on single-crystal samples. *J. Appl. Crystallogr.* **2010**, *43*, 743–751. [CrossRef]
47. Zhao, J.; Angel, R.; Ross, N. The structural variation of rhombohedral $LaAlO_3$ perovskite under non-hydrostatic stress fields in a diamond-anvil cell. *J. Phys. Condens. Matter Inst. Phys. J.* **2011**, *23*, 175901. [CrossRef]

48. Zhuang, Y.; Wu, L.; Gao, B.; Cui, Z.; Gou, H.; Zhang, D.; Zhu, S.; Hu, Q. Deviatoric stress-induced quasi-reconstructive phase transition in ZnTe. *J. Mater. Chem. C* **2020**, *8*, 3795–3799. [CrossRef]
49. Glazer, A.M. The classification of tilted octahedra in perovskites. *Acta Crystallogr. Sect. B Struct. Crystallogr. Cryst. Chem.* **1972**, *28*, 3384–3392. [CrossRef]
50. Glazer, A.M. Simple ways of determining perovskite structures. *Acta Crystallogr. Sect. A* **1975**, *31*, 756–762. [CrossRef]
51. Zhao, Y.; Weidner, D.J.; Parise, J.B.; Cox, D.E. Thermal expansion and structural distortion of perovskite—Data for $NaMgF_3$ perovskite. Part I. *Phys. Earth Planet. Inter.* **1993**, *76*, 1–16.
52. Birch, F. Finite strain isotherm and velocities for single-crystal and polycrystalline NaCl at high pressures and 300 K. *J. Geophys. Res.* **1978**, *83*, 1257–1268.
53. Angel, R.J.; Gonzalez-Platas, J.; Alvaro, M. EosFit7c and a Fortran module (library) for equation of state calculations. *Z. Fur Krist.* **2014**, *229*, 405–419. [CrossRef]
54. Horiuchi, H.; Ito, E.; Weidner, D.J. Perovskite-type $MgSiO_3$; single-crystal X-ray diffraction study. *Am. Mineral.* **1987**, *72*, 357–360.
55. Kudoh, Y.; Ito, E.; Takeda, H. Effect of pressure on the crystal structure of Perovskite-Type $MgSiO_3$. *Phys. Chem. Miner.* **1987**, *14*, 350–354. [CrossRef]
56. Zhao, Y.; Parise, J.B.; Wang, Y.; Kusaba, K.; Vaughan, M.T.; Weidner, D.J.; Kikegawa, T.; Chen, J.; Shimomura, O. High-pressure crystal chemistry of neighborite, NaMgFr: An angle-dispersive diffraction study using monochromatic synchrotron X-radiation. *Am. Mineral.* **1994**, *79*, 615–621.
57. Andrault, D.; Poirier, J.P. Evolution of the distortion of perovskites under pressure: An EXAFS study of $BaZrO_3$, $SrZrO_3$ and $CaGeO_3$. *Phys. Chem. Miner.* **1991**, *18*, 91–105. [CrossRef]
58. Wu, X.; Qin, S.; Gu, T.T.; Yang, J.; Manthilake, G. Structural and elastic properties of $CaGeO_3$ perovskite at high pressures. *Phys. Earth Planet. Inter.* **2011**, *189*, 151–156. [CrossRef]
59. Jung, D.Y.; Oganov, A.R. Ab initio study of the high-pressure behavior of $CaSiO_3$ perovskite. *Phys. Chem. Miner.* **2005**, *32*, 146–153. [CrossRef]
60. Li, L.; Weidner, D.J.; Brodholt, J.; Alfè, D.; Price, G.D.; Caracas, R.; Wentzcovitch, R. Phase stability of $CaSiO_3$ perovskite at high pressure and temperature: Insights from ab initio molecular dynamics. *Phys. Earth Planet. Inter.* **2006**, *155*, 260–268. [CrossRef]
61. Zhao, J.; Ross, N.L.; Angel, R.J. Tilting and distortion of $CaSnO_3$ perovskite to 7 GPa determined from single-crystal X-ray diffraction. *Phys. Chem. Miner.* **2004**, *31*, 299–305. [CrossRef]
62. Wu, X.; Qin, S.; Wu, Z. Generalized gradient approximation calculations of the pressure-induced phase transition of $YAlO_3$ perovskite. *J. Phys. Condens. Matter* **2006**, *18*, 3907–3916. [CrossRef]
63. Ross, N.L.; Zhao, J.; Angel, R.J. High-pressure single-crystal X-ray diffraction study of $YAlO_3$ perovskite. *J. Solid State Chem.* **2004**, *177*, 1276–1284. [CrossRef]
64. Bass, J.D. Elasticity of single-crystal $SmAlO_3$, $GdAlO_3$ and $ScAlO_3$ perovskites. *Phys. Earth Planet. Inter.* **1984**, *36*, 145–156. [CrossRef]
65. Xiao, W.; Tan, D.; Zhou, W.; Liu, J.; Xu, J. Cubic perovskite polymorph of strontium metasilicate at high pressures. *Am. Miner.* **2013**, *98*, 2096–2104. [CrossRef]
66. Hoshino, M.; Sanematsu, K.; Watanabe, Y. Chapter 279—REE Mineralogy and Resources. In *Handbook on the Physics and Chemistry of Rare Earths*; Jean-Claude, B., Vitalij, K.P., Eds.; Elsevier: Amsterdam, The Netherlands, 2016; Volume 49, pp. 129–291.
67. Bouvier, P.; Kreisel, J. Pressure-induced phase transition in $LaAlO_3$. *J. Phys. Condens. Matter* **2002**, *14*, 3981. [CrossRef]
68. Zhao, J.; Ross, N.L.; Angel, R.J. Polyhedral control of the rhombohedral to cubic phase transition in $LaAlO_3$ perovskite. *J. Phys. Condens. Matter* **2004**, *16*, 8763–8773. [CrossRef]
69. Carpenter, M.A.; Sinogeikin, S.V.; Bass, J.D.; Lakshtanov, D.L.; Jacobsen, S.D. Elastic relaxations associated with the—Transition in $LaAlO_3$: I. Single crystal elastic moduli at room temperature. *J. Phys. Condens. Matter* **2010**, *22*, 035403. [CrossRef] [PubMed]
70. Zhao, J.; Ross, N.L.; Angel, R.J.; Carpenter, M.; Howard, C.J.; Pawlak, D.; Lukasiewicz, T. High-pressure crystallography of rhombohedral $PrAlO_3$ perovskite. *J. Phys. Condens. Matter Inst. Phys. J.* **2009**, *21*, 235403. [CrossRef]
71. Verma, A.K.; Modak, P. Ab-initio investigations of $R\bar{3}c$ to $Pm\bar{3}m$ transition in $RAlO_3$ (La, Pr and Nd) perovskites under pressure. *AIP Conf. Proc.* **2013**, *1512*, 86–87. [CrossRef]
72. Liebermann, R.C.; Jones, L.E.A.; Ringwood, A.E. Elasticity of aluminate, titanate, stannate and germanate compounds with the perovskite structure. *Phys. Earth Planet. Inter.* **1977**, *14*, 165–178. [CrossRef]
73. Kung, J.; Rigden, S. Oxide perovskites: Pressure derivatives of the bulk and shear moduli. *Phys. Chem. Miner.* **1999**, *26*, 234–241. [CrossRef]